Title

Synthesis and characterization of aluminum diboride products using 27Al, 11B NMR and ab initio studies

Permalink

https://escholarship.org/uc/item/1pn5478d

Journal

Journal of Materials Science, 53(5)

ISSN

0022-2461

Authors

Turner, Christopher L
Koumoulis, Dimitrios
Li, Gang
et al.

Publication Date

2018-03-01

DOI

10.1007/s10853-017-1727-9

J Mater Sci (2018) 53:3309–3322

Chemical routes to materials

Synthesis and characterization of aluminum diboride products using ^{27}Al, ^{11}B NMR and ab initio studies

Christopher L. Turner[1], Dimitrios Koumoulis[2,*], Gang Li[2], Zoran Zujovic[3], R. E. Taylor[1,*], and Richard B. Kaner[1,4]

[1] Department of Chemistry and Biochemistry, University of California, Los Angeles, Los Angeles, CA 90095-1569, USA
[2] School of Physical Science and Technology, ShanghaiTech University, Shanghai 201210, China
[3] NMR Centre, School of Chemical Sciences, University of Auckland, Private Bag 92019, Auckland, New Zealand
[4] Department of Materials Science and Engineering and California NanoSystems Institute, University of California, Los Angeles, Los Angeles, CA 90095-1595, USA

Received: 3 July 2017
Accepted: 17 October 2017

ABSTRACT

Understanding different bonding environments in various metal borides provides insight into their structures and physical properties. Polycrystalline aluminum diboride (AlB_2) samples have been synthesized and compared both with a commercial sample and with the literature. One issue that arose is the relative ease with which boron-rich and aluminum deficient phases of aluminum borides can be presented in AlB_2. Here, we report ^{27}Al, ^{11}B nuclear magnetic resonance (NMR) spectroscopy and first-principles calculations on AlB_2 in order to shed light on these different bonding environments at the atomic level and compare the structural and electronic properties of the products of different preparations. Along with the aforementioned, the present study also takes an in-depth look at the nature of the ^{11}B and ^{27}Al nuclear spin–lattice relaxation recovery data for the AlB_2 and other superhard materials. The nuclear spin–lattice relaxation has been measured for a static sample and with magic-angle spinning. The combination of NMR and band structure calculations highlights the synthetic challenges with superhard materials.

Introduction

Boron interacts with metals to produce compounds with a variety of structures. For example, at least five different binary compounds formed between tungsten and boron have been reported: W_2B, WB (two crystal structures), WB_2, W_2B_4 (formerly described as W_2B_5), and WB_4 [1–4]. Metal borides also exhibit a range of interesting physical properties, including superconductivity [5] and superhardness [6]. Understanding the different bonding environments in the various metal borides provides insight into the structures and their physical properties. Nuclear magnetic resonance (NMR) spectroscopy can provide information on these different bonding environments at the atomic level.

Address correspondence to E-mail: dkoumoulis@shanghaitech.edu.cn; taylor@chem.ucla.edu

https://doi.org/10.1007/s10853-017-1727-9

We began this series of investigations with a ^{10}B and ^{11}B NMR study of elemental boron [7], which has interesting properties of its own and also provides insight into boron-rich metal boride phases. This was followed by ^{11}B studies of ReB_2 [8] and WB_2 [9]. The experimental NMR details are discussed in depth in these studies. In particular, the ^{11}B quadrupolar frequencies, ν_Q, at 275 kHz for ReB_2 and even less for WB_2, are small enough [9] for the radio frequency (RF) pulse to excite the full ^{11}B resonance, including the satellite transitions. Such considerations are important in spin–lattice relaxation measurements. In conductors such as the metal borides, the spin–lattice relaxation rate provides information on the density of states at the Fermi level.

We now report the results of our investigation of aluminum diboride, AlB_2. The structural motif of AlB_2 differs from that of ReB_2 and WB_2. In the AlB_2 type [10] structure, the layers of boron atoms form flat hexagonal rings. The boron layers are separated by planes of metal atoms in which the metal atoms are located between the centers of two hexagonal boron rings. Each metal atom interacts with six boron atoms in the boron plane above the metal atom and with six boron atoms in the boron plane below the metal atom.

Aluminum diboride further differs from ReB_2 in that both the metal and the boron atoms are easily amenable to study by NMR. Several NMR investigations of AlB_2 have been previously reported [11–18]. However, while there is but a single aluminum site [10] in AlB_2, the literature for AlB_2 shows spectra with a single ^{27}Al NMR resonance, but at three different reported shifts of 1640 ppm [12], 880 ppm [13, 15, 17], and 100 ppm [18]. In general, there has been more agreement among the various studies for the ^{11}B shift.

Along with the issue of the observed ^{27}Al shifts reported for AlB_2, the present study also takes an in-depth look at the nature of the nuclear spin–lattice relaxation recovery data for the quadrupolar nuclei in this compound. Specifically with regard to the experimental NMR parameters, the larger ^{11}B quadrupolar frequency, ν_Q, at 540 kHz in AlB_2 prevents the RF pulse from fully exciting the entire ^{11}B resonance. Remarkably, the ^{11}B spin–lattice relaxation data from a single-pulse saturation experiment were better fit with the "slow irradiation" model rather than the "fast irradiation" model. Obtaining the characteristic spin–lattice relaxation time under these experimental conditions has been examined with various pulse techniques on both static samples and samples studied with magic-angle spinning (MAS).

Experimental

Aluminum diboride, AlB_2, was first synthesized from the elements, amorphous boron (Strem, USA) and aluminum powder (Strem, USA), using an electric arc furnace in a manner similar to that previously described for ReB_2 [8]. A second sample was prepared in a tube furnace reaction using aluminum metal powder (Strem, USA) and amorphous boron (Strem, USA) sealed in a quartz ampule, with a slight excess of boron (nominally $AlB_{2.2}$). The ampule was placed in the tube furnace, heated to 910 °C, and held at this temperature for 12 h before cooling back to ambient temperature. A third sample of AlB_2, commercially available, was purchased from Sigma-Aldrich. The synthetic preparation of the commercial sample differs from our preparations, involving a reaction between aluminum metal and boron trioxide (B_2O_3).

The first sample produced via arc melting contained a slight excess of boron ($AlB_{2.3}$), and the sample was flipped and re-arced to promote homogeneity. The samples were ground to fine powders in a Plattner-style mortar and pestle and washed with dilute HCl to remove any iron contamination introduced during grinding. Utilizing powder X-ray diffraction (pXRD), with an X'Pert Pro diffractometer PANalytical (Netherlands), the arc-melted sample was found to contain aluminum diboride (AlB_2), significant aluminum metal, and other boron-rich aluminum boride phases (AlB_{12}, AlB_{31}). These results suggest incomplete mixing/reaction between the elements during the arc-melting process.

The second sample produced in the tube furnace reaction underwent pXRD analysis, which indicated phase-pure AlB_2, with smaller amounts of aluminum metal and Al_2O_3. The observed aluminum oxide may arise from surface oxidation of the aluminum metal.

The commercially available sample was analyzed using pXRD, and showed phase-pure AlB_2, with both aluminum metal and aluminum oxide (Al_2O_3). In this case, some of the aluminum oxide may correlate with the synthesis method used commercially (i.e., reacting aluminum metal with B_2O_3). This would be in addition to the aluminum oxide arising from the aluminum metal surface. For experimental purposes, the tube furnace AlB_2 product is most similar to the Sigma-Aldrich sample. All the pXRD spectra are shown in Fig. 1. It should also be noted that ^{27}Al NMR spectra [14, 17, 18] previously in the literature for AlB_2 indicate the presence of significant aluminum metal in the samples. Due to the presence of aluminum metal in all of these samples (including the literature reports), there was interest in comparing the spectra of the products from different preparations.

The NMR data were acquired with a Bruker DSX-300 spectrometer using both magic-angle spinning (MAS) and wideline techniques. Nuclei observed included ^{11}B at a frequency of 96.29 MHz, ^{23}Na at 79.39 MHz, ^{27}Al at 78.20 MHz, and ^{207}Pb at 62.79 MHz. The NMR samples were ground to − 325 mesh (< 44 μm) to minimize radio frequency (RF) skin-depth effects. Due to the conductivity [11] of AlB_2 (reported to be "not very different, and perhaps even greater, than that of aluminum metal (skin depth = 19 μm at 20 °C"), each sample was also mixed with an equal volume of NaCl to reduce particle-to-particle contact. The mixing with NaCl provided significant improvements in both the tuning of the NMR probes and in achieving higher MAS sample spinning rates. For sample temperature measurements [19–21], one AlB_2 sample was mixed with an equal volume of $PbNO_3$ instead of NaCl.

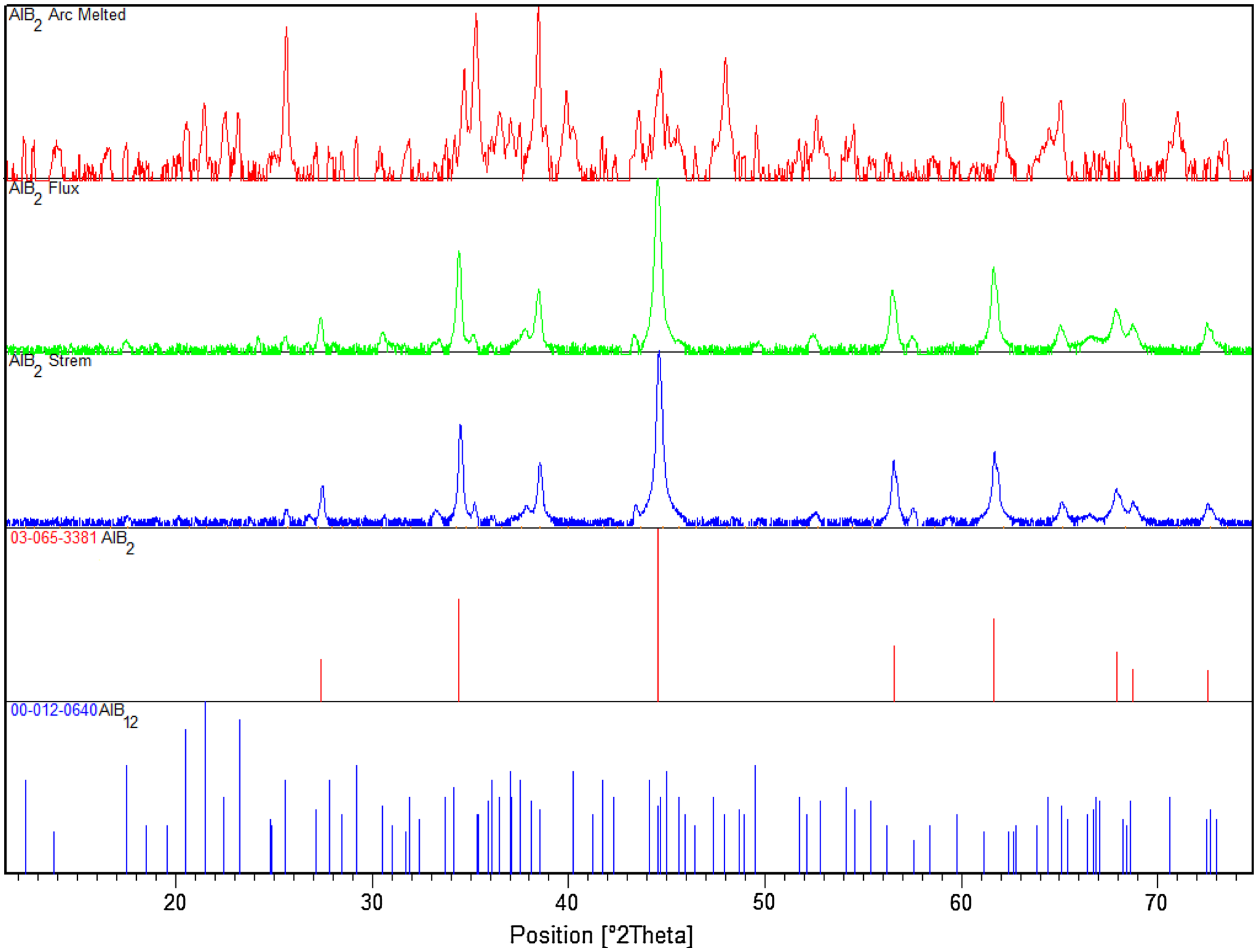

Figure 1 X-ray diffractograms for experimentally produced AlB_2 samples (top 3 spectra): arc melted (red), flux growth (green), and Strem chemical (blue); the bottom line patterns are JCPDS references for AlB_2 03-065-3381 (red) and AlB_{12} 00-012-0640 (blue). The arc-melted sample (top red) contained predominantly AlB_2 and AlB_{12}, but also contained aluminum metal and higher boride species (e.g., AlB_{66}). The flux grown sample (blue) contained trace amounts of aluminum metal; the commercially available sample contained traces of aluminum oxide, residual from the synthetic process.

MAS spectra of the aluminum diboride powder mixed with either NaCl or $PbNO_3$ were acquired with a standard Bruker MAS probe using a 4-mm outside diameter zirconia rotor with a sample spinning rate of either 5 or 12.3 kHz. The ^{11}B $\pi/2$ pulse width for the MAS experiments was 5 µs as measured on an aqueous solution of boric acid. The ^{11}B background from the boron nitride stator in the MAS probe was minimized by the use of the Elimination of Artifacts in NMR SpectroscopY (EASY) pulse sequence [22]. The ^{27}Al $\pi/2$ pulse width was 9 µs as measured on an aqueous solution of $AlCl_3$. The ^{23}Na $\pi/2$ pulse width was 3 µs as measured on an aqueous solution of NaCl. The ^{207}Pb $\pi/2$ pulse width was 9 µs.

A static sample of the aluminum diboride powder mixed with NaCl was placed in a standard Bruker X-nucleus wideline probe with a 5-mm solenoid coil with the sample confined to the length of the RF coil. The use of a polyimide coil support and a quartz sample tube removed any ^{11}B background that might arise from the presence of sodium borosilicate glass. The ^{11}B $\pi/2$ pulse width was 5 µs as measured with an aqueous boric acid standard. For both the MAS and wideline probes, the "solid-state" 90-*degree* pulse width was reduced by a factor of (I + ½), where I is the nuclear spin, in comparison with the 90-*degree* pulse width for the same nucleus measured in solution [23, 24].

The NMR spectral data were acquired by either single-pulse (with a dead time of 8.5 µs) or a quadrupolar echo sequence [25] with an interpulse spacing, τ, of 15 µs. The ^{11}B NMR spectra were acquired with a delay of five times the spin–lattice relaxation time (T_1) as determined by a saturation-recovery technique [26]. In the various ^{11}B saturation-recovery experiments, three different saturation methods were used. These included either a single-pulse saturation or a pulse sequence of ($p3_x$ − 130 µs–$p3_y$ − 150 µs–$p3_{-x}$ − 141 µs–$p3_{-y}$ − 137 µs–) repeated 125 times for a total of 500 RF pulses (p3) applied. The RF pulse p3 was 4.25 µs, a value experimentally determined by minimizing the remaining signal 100 µs after the saturation pulse sequence. The intervening times between the p3 pulses in the saturation sequence are chosen to be longer than the time for the NMR signal to dephase into the noise of the baseline after a single pulse. For the ^{11}B saturation-recovery experiment with MAS at a rate of 5 kHz, the method of pulsing asynchronously to the sample spinning given by Yesinowski [27] was used.

The ^{11}B chemical shift scale was calibrated using the unified Ξ scale [28], relating the nuclear shift to the ^{1}H resonance of dilute tetramethylsilane in $CDCl_3$ at a frequency of 300.13 MHz. The reference compound for defining zero ppm is BF_3 etherate [28]. The chemical shift referencing was experimentally verified with the ^{11}B resonance of an aqueous solution of boric acid [29] at pH 4.4.

Spectral simulations were performed with the solids simulation package (''solaguide'') in the TopSpin (Version 3.1) NMR software program from Bruker BioSpin.

The hexagonal structure of AlB_2 with space group of *P6*/*mmm* was considered in our calculations. The computed lattice constants $a = b = 3.007$ Å and $c = 3.2744$ Å are consistent with the experimental value [30]. The boron atoms locating at B (1/3, 1/6, 1/2) and B (1/6, 1/3, 1/2) form honeycomb layers that are separated by the hexagonal close-packed aluminum. The electronic structure was calculated with the full potential linearized augmented plane wave (LAPW) method implemented in *WIEN2 k* (v16.1) package [31]. The general gradient approximation (GGA) of Perdew et al. [32] was used for exchange–correlation potential. The converged basis corresponds to $R_{\min}K_{\max} = 7.0$, where $R_{\min}$ is the minimum LAPW sphere radius and $K_{\max}$ is the plane wave cutoff. The first Brillouin zone was sampled with 16 × 16 × 12 k-points.

Results and discussion

During the course of this investigation, the challenges of synthesizing metal diborides from "light" main-group elements became apparent. One issue that arose is the relative ease with which boron-rich phases of aluminum borides can be prepared. As powder X-ray diffraction is relatively insensitive to the boron atoms, very long data acquisition times are generally required to fully identify the presence of these "light" main-group boride phases. However, these phases easily manifest themselves by magnetic resonance spectroscopy. The ^{11}B NMR spectrum of a static polycrystalline sample of such boron-rich phases is shown in Fig. 2a. The spectrum is nearly identical to the "two split lines" [33] observed in elemental boron [7], Fig. 2b. Although both the

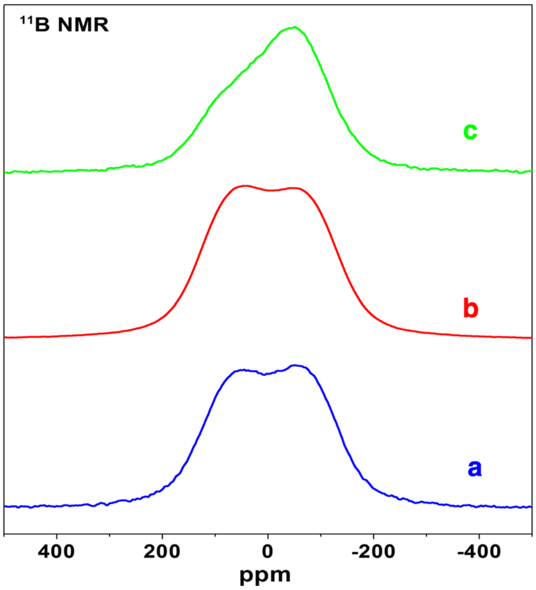

Figure 2 ^{11}B NMR spectra of static polycrystalline samples at ambient temperature of *a* boron-rich phases AlB_{12} and AlB_{31} (bottom), *b* elemental boron (middle), and *c* commercial AlB_2 (top).

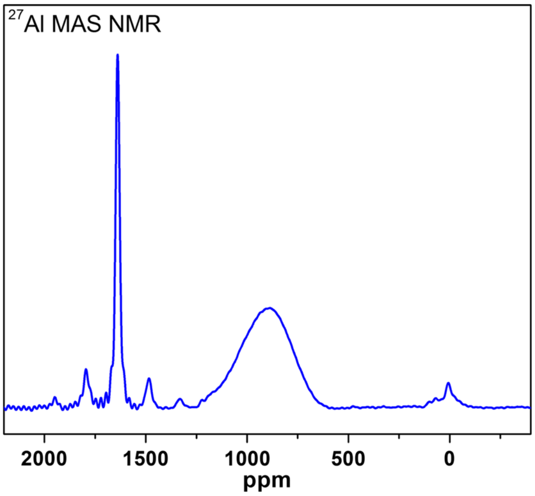

Figure 3 ^{27}Al MAS spectrum of a commercial AlB_2 sample from Sigma-Aldrich.

"second-order quadrupole effect" [33] and "two distinct boron sites" [34] had been proposed in the literature, this spectral effect in elemental boron was demonstrated to arise from isotropic bulk magnetic susceptibility [7]. In elemental boron, partial occupancy of unit cell sites results in defects yielding paramagnetic centers that can be observed by electron paramagnetic resonance (EPR) spectroscopy [7]. EPR spectra (not shown) were also acquired on these boron-rich phases and are nearly identical to those of elemental boron [7].

This point of the relative ease of formation of boron-rich metal borides with the "light" main-group element of aluminum is raised because a very similar "doublet" has been previously reported [13] for MgB_2 and interpreted as a "dipolar doublet." If such a "doublet" arises from isotropic bulk magnetic susceptibility, as in the cases of elemental boron and the boron-rich aluminum boride phases, then the splitting will be dependent upon the particle size [7]. In addition, the sample will yield a measurable EPR spectrum. Such issues as these might provide an alternative explanation for the doublet structure in the MgB_2 spectrum. This will be pursued in a separate publication.

^{27}Al NMR highlights another synthetic challenge with AlB_2. Figure 3 shows the ^{27}Al MAS spectrum of the commercial AlB_2 sample from Sigma-Aldrich that contains three resonances. As mentioned in the "Introduction," the literature for AlB_2 reports three different ^{27}Al shifts at 1640 ppm [12], 880 ppm [13, 15, 17], and 100 ppm [18]. Despite its assignment as the resonance for AlB_2 in Ref. [12], the peak around 1680 ppm, showing spinning sidebands, has been identified as the Knight shift for aluminum metal [35, 36]. The assignment of this peak as attributed to aluminum metal has been experimentally confirmed by the addition of aluminum powder to the sample [14] and is in agreement with the results found here. The peak around 880 ppm, which does not narrow under MAS, is consistent with that assigned as AlB_2 in several studies [13–15, 17]. The peak around 0 ppm could rise from aluminum oxide, presumably from the surface of the aluminum metal particles and from aluminum metal reacting with boron trioxide.

This resonance around 0 ppm differs somewhat in shift from the lone report [18] of 100 ppm as the assignment for the ^{27}Al resonance for AlB_2. However, there is a possible explanation for the observation of a ^{27}Al shift for AlB_2 differing from the numerous reports of a resonance around 880 ppm. X-ray diffraction data and density measurements in previous studies [16, 37] have indicated an Al deficiency in AlB_2. Loa et al. [37] have calculated the band structure and density of states for stoichiometric AlB_2. The π-type bands derived from the boron p_z states and bands with Al-*s* character are partially filled. Based on the rigid-band picture they argued that AlB_2 with a 10% Al deficiency (e.g., $Al_{0.9}B_2$) would result in a removal of 0.3 Al valence electrons, which is sufficient to greatly deplete the number of electrons in the band of Al-*s* states.

To verify this picture, we have carried out a calculation for the 2 × 2 × 2 superstructure of AlB_2 with central Al atom removed, which effectively corresponds to AlB_2 with 12.5% aluminum deficiency, i.e., $Al_{0.85}B_2$. After fully relaxing the internal coordinates of every atom, we calculated the electronic structure and show it in Fig. 4. We found that the 12.5% aluminum deficiency completely removes the electron pocket around *Γ* (Fig. 4b) as claimed in Ref. [37]. However, in contrast to the statement on the complete depletion of the Al-*s* band, we found reasonable amount of bands with Al-*s* character around the Fermi level that are mainly contributed from the H point (Fig. 4a). As a result of the diminished but not complete depletion of the Al-

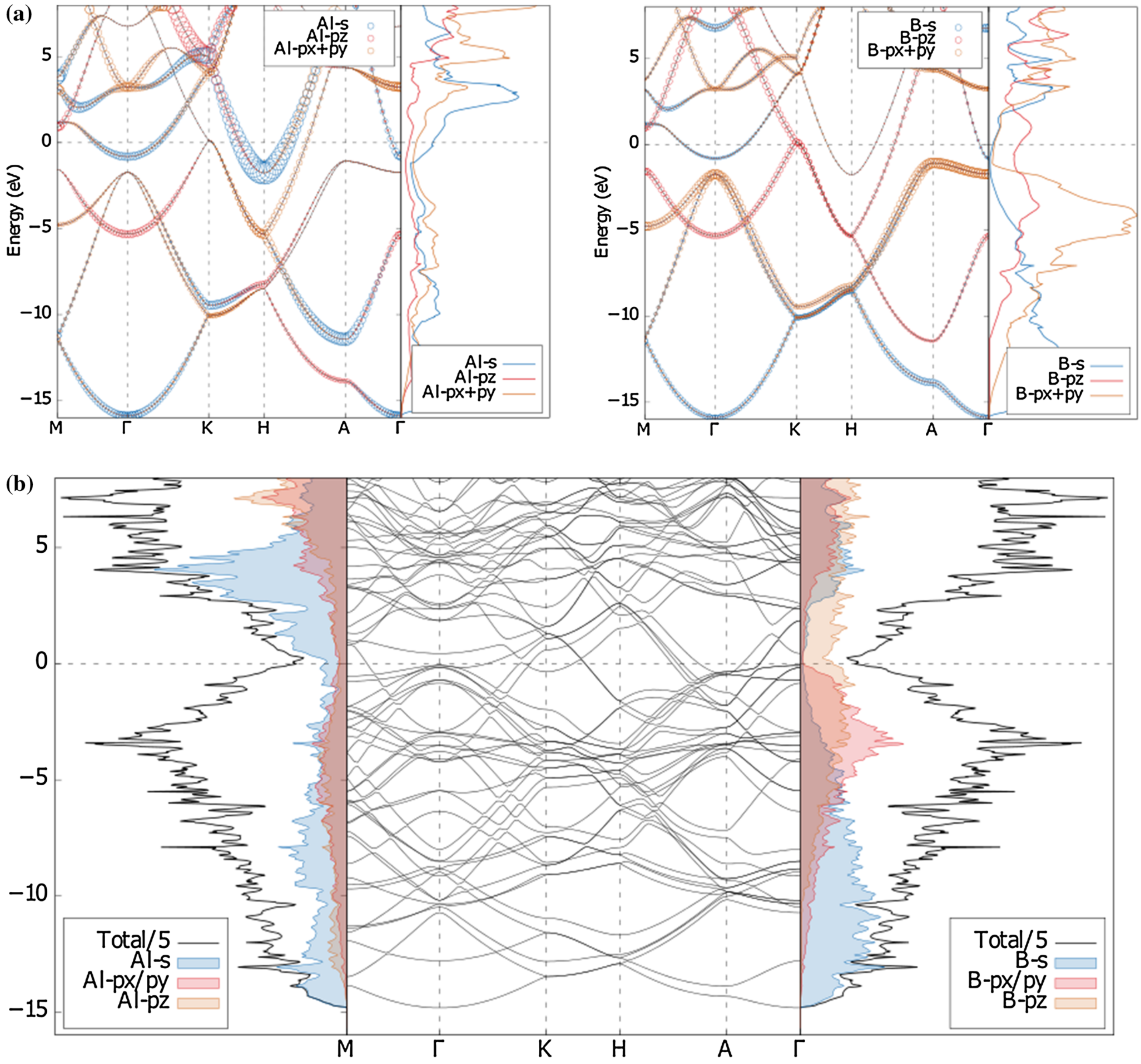

Figure 4 Electronic structure and density of states (DOS) of **a** AlB_2 and **b** $Al_{0.85}B_2$. The orbital projections of Al and B in single AlB_2 unit cell are displayed as circles in (**a**). 12.5% aluminum deficiency in (**b**) is effectively simulated by removing one Al from the 2 × 2 × 2 superstructure of AlB_2. At the left- and right-hand sides of (**b**) the comparison of the atomic- and orbital-resolved DOS to the rescaled total DOS are shown.

s states, a reduction of the ^{27}Al Knight shift would be expected. The observed ^{27}Al shift (Fig. 3) may be dependent upon the aluminum deficiency.

The ^{27}Al MAS spectrum in Fig. 3 was acquired using a single pulse of 0.5 µs in order to provide as quantitative a spectrum as possible [23, 24]. Integration of the spectrum indicates that about 28% of the aluminum atoms are present as aluminum metal and about 67% present as AlB_2. The remaining 5% of the aluminum atoms are present as the oxide. Very similar results were obtained from the AlB_2 sample prepared by the tube furnace method. It should also be noted that the ^{27}Al spectra given in Refs. 14, 17 and 18 all show a significant aluminum metal resonance in addition to that assigned to AlB_2. As can be inferred from these data from these different samples, preparing AlB_2 completely free of aluminum metal is difficult. The inclusion of aluminum metal within the AlB_2 samples makes it difficult to easily identify the metal boride phase by X-ray powder diffraction in such "light" main-group metal borides. As noted above, ^{11}B NMR and EPR spectra can be useful in indicating the presence of boron-rich metal boride phases in the sample.

The ^{11}B and ^{27}Al NMR spectral parameters for AlB_2 are given in Table 1. Figure 5 shows the fit of a shielding anisotropy model to the ^{11}B experimental data. As was previously assumed [16] for ^{11}B in $Al_{0.9}B_2$, the two principal axis systems for the quadrupolar interaction and for the shielding anisotropy are coincident for ^{11}B in AlB_2. The parameters for the quadrupolar interaction were determined from the Variable Offset Cumulative Spectra (VOCS) [38] shown in Fig. 6.

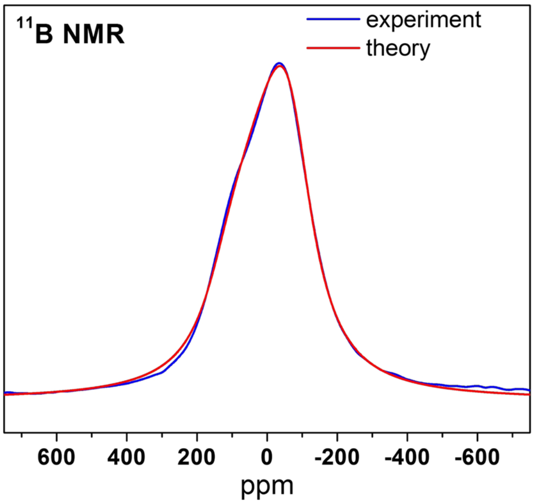

Figure 5 Experimental ^{11}B spectrum of a static sample of AlB_2 is shown in blue. The smooth redline is a simulated fit of a shielding anisotropy model. The extracted parameters are given in Table 1.

The ^{11}B VOCS spectrum in Fig. 6 allows the ^{11}B quadrupolar frequency to be determined directly from the observed spectral satellites in this first-order quadrupolar spectrum. Using this experimental

Table 1 ^{27}Al and ^{11}B NMR quadrupolar and shielding parameters of AlB_2

	δ_{iso},^{a,b} (ppm)	C_Q^c (MHz)	υ_Q^d (MHz)	η_q^e	δ_{11}^b (ppm)	δ_{22}^b (ppm)	δ_{33}^b (ppm)	ζ_{csa}^f (ppm)	η_s^g	Ω^h (ppm)	κ^i
$Al^{11}B_2$ static	− 6.0	1.10	0.550	0	138.5	− 78.3	− 78.3	145	0	217	− 1
$Al^{11}B_2$ MAS	− 7.7										
$^{27}AlB_2$	880	0.533^j	0.080^j								

^{a}Spectral parameters obtained from simulations in Fig. 4

^{b}Shifts referenced to the unified Ξ scale [28]

^{c}Quadrupolar coupling constant $\{e^2qQ/\hbar\}$

^{d}Quadrupolar frequency $\{3e^2qQ/[2I(2I-1)\hbar]\}$

$^e\eta$ = asymmetry $\{0 \le \eta \le 1\}$

$^f\zeta_{csa} = \delta_{33} - \delta_{iso}$

$^g\eta = (\delta_{22} - \delta_{11})/\zeta_{csa}$

$^h\Omega = |\delta_{33} - \delta_{11}|$

$^i\kappa = 3(\delta_{22} - \delta_{iso})/\Omega$

^{j}From Ref. 13

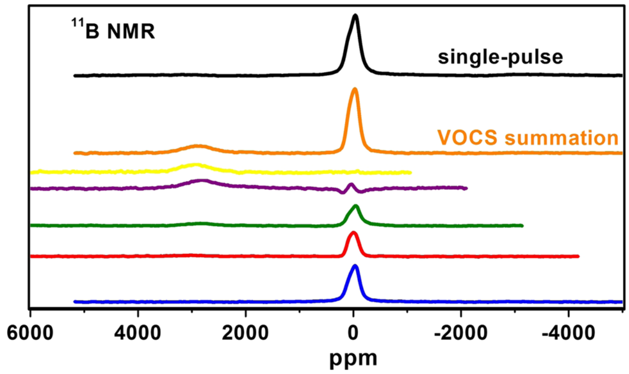

Figure 6 Partial ^{11}B VOCS result for the central and high-frequency satellite transition is shown on the bottom. These spectra were acquired with a quadrupolar echo sequence. The ^{11}B spectrum shown on the top was acquired with a single-pulse acquisition using a dead time of 8.5 µs. The resulting roll in the baseline of the spectrum has been corrected.

value of the quadrupolar frequency, the second-order quadrupolar contribution, with a spectral width of ca. 15 ppm, to the observed central transition lineshape shown in Fig. 5 is almost negligible compared to the full width of the central transition. This observed lineshape and linewidth of the central transition are dominated by the shielding anisotropy, the fit of which is shown in Fig. 5. In this simulation, the second-order quadrupolar interaction in essence provides the broadening function used in the simulation of the shielding anisotropy. These results are in agreement with those previously reported in Ref. 16.

NMR measurements of the spin–lattice relaxation rate provide a probe at the atomic level that yields information on the Fermi surface. For the spin–lattice relaxation of a half-integer quadrupolar nuclei in a non-cubic singe crystal, Andrew and Tunstall [39] showed that relaxation recovery is typically characterized by a multi-exponential function regardless of whether the relaxation mechanism is quadrupolar or magnetic in origin. The derivation assumed that there are no accidental degeneracies of the satellite energy levels with that of the central transition resulting from the crystal orientation in the static magnetic field. The multi-exponential recovery arises from the quadrupolar interaction creating unequal energy spacings in the Zeeman interaction.

The Andrew and Tunstall [39] model for saturation-recovery spin–lattice relaxation derived for magnetic relaxation of spin-3/2 nuclei with selective saturation of the central transition is given by the following equation:

$$\frac{M(\infty) - M(t)}{M(\infty)} = \left(0.4e^{-\frac{t}{T1}} + 0.6e^{-6\frac{t}{T1}}\right) \tag{1}$$

However, the equation that is typically fit to the experimental data "for the case of saturation of the central line of the ^{11}B NMR spectrum with a single rf pulse (or short sequence of pulses and for magnetic relaxation mechanism"^{11} (*cf.*, Refs. 13, 14, 40 and 41) has different coefficients for the two exponential functions

$$\frac{M(\infty) - M(t)}{M(\infty)} = \left(0.1e^{-\frac{t}{T1}} + 0.9e^{-6\frac{t}{T1}}\right) \tag{2}$$

from those found in the Andrew and Tunstall [39] model given in Eq. (1), although the Andrew–Tunstall work is generally cited as the reference for Eq. (2). Usually, no further explanation for the differing equations is given. However, the apparent explanation depends upon the RF irradiation of the central transition [42]. Under the assumption that "the irradiation pulse(s) are chosen so that they disturb only the equilibrium of the central transition without affecting the population of the other energy levels" [42], i.e., "fast irradiation," then the saturation recovery is described by Eq. (2). However, if "the irradiation period is so long that the unperturbed levels will come to thermal equilibrium with the irradiated levels" [42], i.e., "slow irradiation," in this case the saturation recovery is described by Eq. (1). In short, the experimental details of the spin–lattice relaxation experiment are important in extracting a time constant for data analysis.

For nuclear spin–lattice relaxation experiments of half-integer quadrupolar nuclei, the radio frequency pulses that are used in the experiment need to be characterized. For the ^{11}B relaxation measurements performed with a static sample of AlB_2 in the wide-line probe, the ^{11}B $\pi/2$ pulse width first was measured with an aqueous boric acid standard and determined to be 5 µs. Using the 360-*degree* pulse width gives a radio frequency field, ν_{RF}, of 50 kHz. In this case, the ν_{RF} is an order of magnitude smaller than the quadrupolar frequency, ν_Q, of 540 kHz previously reported for ^{11}B in AlB_2 [11, 13, 16]. For ^{11}B spectral acquisitions by either single-pulse or quadrupolar echo sequences (τ = 15 µs), the "solid-state" 90-*degree* pulse width [23, 24], reduced by a factor of (I + ½) = 2 where I is the nuclear spin, of 2.5 µs was used. Under these experimental conditions using a quadrupolar echo sequence, the RF pulse appears to be relatively "selective," as shown in the VOCS [38] given in Fig. 6. Specifically, RF excitation of the central transition shows no spectral intensity at the spectral singularity associated with the higher frequency satellite transition. Alternatively, RF excitation of the spectral singularity associated with the higher frequency satellite transition shows no intensity of the central transition. In comparison with the quadrupolar-echo spectra, the single-pulse spectrum acquired with a ringdown delay (or "deadtime") of 8.5 µs is shown in the top trace of Fig. 6. It should be noted that the baseline roll arising from the ringdown delay in this spectrum has been corrected. The single-pulse spectrum also suggests that the RF pulse is relatively "selective" in that the satellite transitions are not readily observed.

Although both $\nu_{RF} << \nu_Q$ and the absence of spectral intensity of the singularity of the satellite transitions in the one-dimensional spectra when the RF is located at the central transition suggest that this experimental RF is relatively selective, this RF pulse is still able to excite nuclei much further away than the 50 kHz RF field might suggest. This effect is demonstrated with the ^{27}Al spectrum shown in Fig. 7. For the ^{11}B and ^{27}Al spectra of AlB_2 in this study, the AlB_2 samples were mixed with equal volumes of NaCl to minimize RF skin-depth issues with the conductive AlB_2, as described in the Experimental methods. With the wideline probe, the ^{27}Al $\pi/2$ pulse width was 9 µs as measured on an aqueous solution of $AlCl_3$. The "solid-state" 90-*degree* pulse width is 3 µs as ^{27}Al is a spin-5/2 nucleus. The ^{27}Al spectrum shown in Fig. 7 is from a sample of pure NaCl. The ^{27}Al signal around 0 ppm is a background signal from aluminum contained in the ceramic surrounding the RF coil in the wideline probe. In this case, ^{27}Al resonates at 78.172 MHz. The signal around 2395 ppm is an aliased ^{23}Na resonance from NaCl that resonates at 79.353 MHz, as evidenced by simply acquiring the same spectrum with an empty probe. In this case, the spectral width is 1 MHz, acquired with the shortest available dwell time of 0.5 µs. No filtering, either electronically or digitally, was used in the acquisition of the time domain signal. The ^{23}Na signal is aliased in from the right-hand side of the spectrum. The frequency range excited by a square RF pulse can be approximated by the Fourier transformation of a square, i.e., a sinc function [43]. The bandwidth for this frequency distribution is 1.2/(pulse width) Hz [43]. The "solid-state" 90-*degree* pulse width of 3 µs has a bandwidth of 0.4 MHz. However, excitation of the ^{23}Na resonance 1.166 MHz away from the ^{27}Al resonance occurs, as shown in Fig. 7. It should be noted that the bandwidth as given by the Fourier transformation takes into account only the pulse width (and not the RF power). As such, this bandwidth will differ from that of the radio frequency field, ν_{RF}, which is based on the 360-*degree* pulse width. This ability to affect nuclear spins beyond the expected bandwidth comes into play in the measurement of ^{11}B spin–lattice relaxation times.

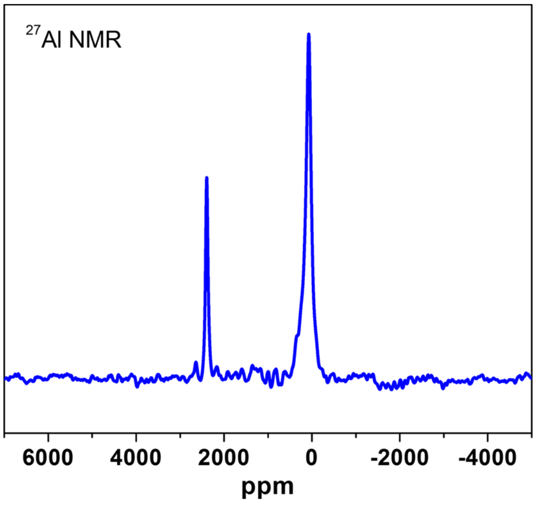

Figure 7 ^{27}Al NMR spectrum acquired using a pure NaCl sample with a wideline probe.

As noted above, the RF pulses can excite nuclei well beyond the expected bandwidth, although this may not be immediately evident in the one-dimensional spectra. This effect manifests itself in the ^{11}B saturation-recovery data shown in Fig. 8. Data sets for three different ^{11}B saturation-recovery experiments obtained from the Sigma-Aldrich AlB_2 are shown. The relaxation data sets in Fig. 8 show data covering variable delays spanning five orders of magnitude.

The first data set in Fig. 8 is from a saturation-recovery experiment using a single pulse of 4.5 µs for saturation of a static sample of AlB_2. As can be seen, the experimental data are much better fit by the Andrew and Tunstall [39] model given in Eq. (1) rather than that by the "fast irradiation" model for a single pulse given in Eq. (2). The second experimental data set is also for a static sample. However, instead of a single RF pulse for saturation, a pulse train pulse of ($p3_x$ – 130 µs–$p3_y$ – 150 µs–$p3_{-x}$ – 141 µs–$p3_{-y}$ – 137 µs–) repeated 125 times

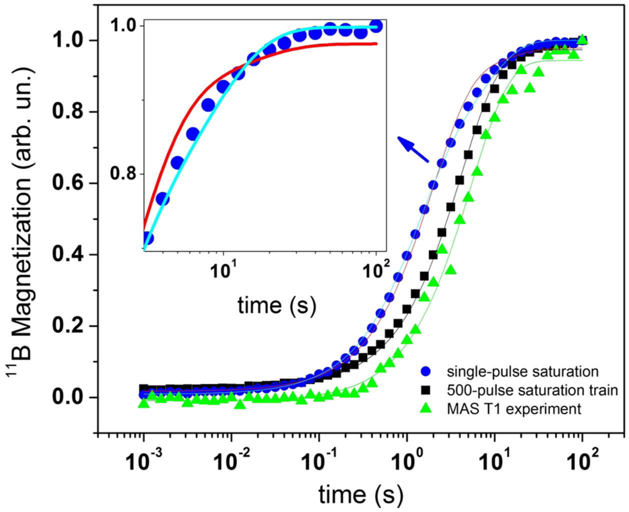

Figure 8 ^{11}B NMR saturation-recovery spin–lattice relaxation data obtained from a single-pulse saturation (blue circles), a 500-pulse saturation train (black squares) and Yesinowski's [27] MAS technique. For the single-pulse saturation, the data have been fitted with both the slow irradiation (Andrew–Tunstall) and fast irradiation models (see text for discussion).

for a total of 500 RF pulses (p3) was applied. The third experimental data set was acquired with the technique of Yesinowski [27] using MAS at 5 kHz. In this MAS technique for measuring the spin–lattice relaxation time, a train of saturation pulses is applied asynchronously to the MAS in order to use the overlapping of the satellite and central transitions during the sample rotation so that both central and satellite transitions are saturated. It should be noted that all three techniques significantly saturate the ^{11}B magnetization. This is in contrast to the ^{11}B saturation-recovery experiments for ReB_2 [8] in which approximately 8% of the ^{11}B magnetization remained after applying the saturation technique.

Applying the models to the various data sets in Fig. 8 with delays spanning five orders of magnitude can yield time constants from the fits that differ significantly from each other. It should also be noted that the first two data sets cannot be well fit with a single exponential function. For the first data set shown in Fig. 8, the recovery data are obtained with a single saturation pulse of 4.5 μs, a value experimentally determined by minimizing the remaining signal 100 μs after the saturation pulse. In contrast to "the case of saturation of the central line of the ^{11}B NMR spectrum with a single rf pulse (or short sequence of pulses and for magnetic relaxation mechanism" [13], Eq. (2) does not fit the experimental data nearly as well as the Andrew and Tunstall [39] model given by Eq. (1). The Andrew–Tunstall model yields a T_1 of 6.8 s. However, the "fast irradiation" [42] of Eq. (2) is primarily composed of the exponential with a time constant of $T_1/6$. As a result, the (poorer) fit of Eq. (2) to the experimental data yields a significantly longer T_1 of 11.1 s. The important point is that the choice of mathematical model significantly affects the extracted time constant. In this case, the difference is almost a factor of two. The better fit of the Andrew–Tunstall model to the experimental data over that of the "fast irradiation" model suggests that the single RF pulse used for saturation affected the population of the other energy levels [42] rather than simply those of the central transition. Such a result is consistent with the observed fact that RF pulses used in this study excited nuclei well beyond the "RF field" or "RF bandwidth" determined from Fourier transform theory. The appropriate initial populations of the central and satellite transitions for application of the "fast irradiation" model are not created by the RF pulse used in the saturation-recovery experiment. As a result, an erroneous time constant is extracted.

This excitation effect of the RF pulses is further illustrated in the data set obtained using a saturation pulse train pulse of ($p3_x - 130$ μs–$p3_y - 150$ μs–$p3_{-x} - 141$ μs–$p3_{-y} - 137$ μs–) repeated 125 times for a total of 500 RF pulses (p3). The spin–lattice saturation recovery as shown in Fig. 8 obviously takes longer than that for the application of a single RF pulse. Fitting this data set with a single exponential function with a time constant of T_1 yields a time constant of 4.3 s. That is, the application of multiple pulses for saturation is beginning to saturate the satellite transitions. For the case of full saturation of the central transition and the satellite transitions, a saturation recovery characterized by a single exponential function would be expected [8, 27]. The T_1 of 4.3 s form the pulse train saturation is shorter than the 6.8 s obtained from fitting the Andrew–Tunstall model to the single-pulse saturation data. This pulse sequence does not fully saturate the satellite transitions. As a result, the extracted time constant is not correct.

Finally, for comparison, fitting the saturation-recovery data acquired with the technique of Yesinowski [27] using MAS at 5 kHz with a single exponential function gives a T_1 of 5.5 s. The effects of spinning a conductive sample in a magnetic field, including both heating and braking, have been previously studied for CuI [44]. To check for these effects, the − 325 mesh AlB_2 sample was also mixed with an equal volume of $PbNO_3$. Monitoring of the ^{207}Pb chemical shift [19–21] at a MAS spinning rate of 5 kHz indicated only a modest 3.6 K increase in sample temperature over that of the static sample. This is the small temperature increase expected from frictional heating of the sample under MAS at this spinning rate. With the small particles dispersed in the $PbNO_3$, there is no experimental evidence of sample heating due to the conductivity nor is there any evidence from the drive gas pressure required of any magnetic braking effect.

The ^{27}Al spin–lattice relaxation times were measured with a saturation-recovery experiment using a static sample. The comparatively small value of ν_Q of 80 kHz for aluminum in AlB_2 [13] means that the full ^{27}Al resonance, including satellite transitions, can be saturated with the radio frequency pulse. As a result, the saturation-recovery data are characterized by a single exponential function. At 294 K, the measured ^{27}Al spin–lattice relaxation time was 13 ms and ranged from 35 ms at 148 K to 8 ms at 423 K. The relaxation data as a function of temperature yield a Korringa product of $(T_1 * T) = 4.1$ sK. By using the spectral shift of 880 ppm, the Korringa ratio was estimated to be $R = \frac{K^2 T_1 T}{S} = 0.82$ where $S = (\gamma_e/\gamma_n)^2 (h/8\pi^2 k_B)$ for ^{27}Al nucleus. The obtained ratio is close to unity suggesting that the nuclear spin–lattice relaxation mechanism can be described by the contribution of *s*-type carriers. However, based on our theoretical calculations both *s* and *p* states coexist at the Fermi level almost in an equal amount $[N_s^{Al}(E_F) = 0.058$ states/eV f.u. and $N_p^{Al}(E_F) = 0.043$ states/eV f.u.$]$ which can explain the value of the Korringa ratio to be closer to unity but less than it. This interesting result reveals the high sensitivity of the NMR parameters on both the total and partial DOS at the E_F. Applying now the same analysis on the ^{11}B relaxation data, the Korringa ratio found to be very small 0.023 that experimentally verifies the primacy of the *p* electrons at the partial DOS of boron sites in AlB_2 $[N_p^B(E_F) = 0.330$ states/eV f.u.$]$. The estimated orbital and Fermi-contact contributions in both nuclei are in conformity with the ab initio calculations as predicted for the partial density of states at the E_F for ^{27}Al $N_s^{Al}(E_F) = 0.058$ states/eV f.u. and for ^{11}B $N_s^B(E_F) = 0.004$ states/eV f.u. (see Fig. 4 and Table 2).

Table 2 Total and Al and B partial DOS at the Fermi level in units of states/eV f.u. for AlB_2

Alloy	N_s (E_F)	N_{p_z} (E_F)	$N_{p_{xy}}$ (E_F)
Pure AlB_2 total	0.062	0.339	0.034
B	0.004	0.324	0.006
Al	0.058	0.015	0.028
Al-deficient AlB_2 total	0.026	0.039	0.016
B	0.002	0.031	0.001
Al	0.024	0.008	0.015

The ^{27}Al spin–lattice relaxation rate was also measured for aluminum metal by using the resonance at 1680 ppm. The face-centered cubic aluminum lattice [45] requires the quadrupolar interactions to vanish by symmetry. As a result, the saturation-recovery data of aluminum metal are also characterized by a single exponential function. At 294 K, the measured ^{27}Al spin–lattice relaxation time was 2.4 ms, which may be compared with the reported [46] 6 ms measured at ambient temperature at a frequency of 16 MHz. The measured ^{27}Al spin–lattice relaxation times ranged from 5.6 ms at 148 K to 1.6 ms at 423 K. The relaxation data as a function of temperature yield a product of $(T_1 * T) = 0.84$ sK, which is smaller than the previously reported [45] value of 1.85 sK.

For completeness to further illustrate spin–lattice relaxation behavior for quadrupolar nuclei, as ^{23}Na is similar to ^{11}B in being a spin-3/2 quadrupolar nucleus, the ^{23}Na spin–lattice relaxation for NaCl was also characterized. Sodium chloride crystallizes in a face-centered cubic lattice, with each ion surrounded by an octahedron of the oppositely charged ion. As a result of the cubic symmetry, the static quadrupolar interaction is zero. The ^{23}Na spin–lattice relaxation in a single crystal [47] was previously investigated at frequencies of 4.5 MHz and 12 MHz. Relaxation time constants, T_1, of 12 s at 298 K, 14.5 s at 273 K, and 28 s at 195 K were reported, which established the relaxation mechanism as quadrupolar (rather than magnetic) with van Kranendonk's theory [48]. Additionally, the study was specifically able to rule out the role of paramagnetic centers as playing a role in the nuclear spin relaxation. No dependence of T_1 upon crystal orientation with respect to the magnetic field was observed. In our experiments, the ^{23}Na saturation-recovery data for a static sample of polycrystalline NaCl at 295 K measured at 79.39 MHz were well fit with a single exponential function that yielded a T_1 of 14.4 s. An inversion-recovery experiment, also well fit by a single exponential function, yielded a T_1 of 13.9 s. Finally, a fit of a single exponential function to the ^{23}Na inversion-recovery data for the same sample of polycrystalline NaCl at 295 K undergoing MAS yielded a T_1 of 14.1 s. As expected, with cubic symmetry such that only the central transition is observed, MAS does not change the ^{23}Na T_1. For the static sample, the full width at half maximum is 2.78 kHz while the MAS spectrum gives a narrowed resonance with a full width at half maximum of 38 Hz.

Conclusions

For pure and Al-deficient AlB_2, ab initio calculations and NMR parameters characterizing both the density of states at the Fermi level, the electric field gradient and the shielding at both the boron and aluminum sites are presented. Band structure results reveal that aluminum deficiency completely removes the electron pocket around Γ of the band structure. However, in contrast to previous calculations, we found that a reasonable amount of bands with Al-*s* character around the Fermi level remain and mainly contribute from the H point. To verify this picture, ^{11}B and ^{27}Al spectral analysis and nuclear spin–lattice relaxation experiments were carried out for all samples with various pulse techniques. Characterization of the radio frequency pulses used in the relaxation measurements indicates that nutation frequencies are small in comparison with the quadrupolar interaction at the ^{11}B site. Interestingly, in contrast to expectations, the ^{11}B spin–lattice relaxation data from a single-pulse saturation experiment were better fit with the “slow irradiation” model rather than the “fast irradiation” model.

Acknowledgements

This material is based upon work supported by the National Science Foundation Grants DMR-9975975 (R.E.T.), DMR-1506860 (R.B.K.) and ShanghaiTech University Start-up Funding. The authors would like to thank Georgiy Akopov for assistance with flux growth.

References

[1] Kayhan M, Hildebrandt E, Frotscher M, Senyshyn A, Hofmann K, Alff L, Albert B (2012) Neutron diffraction and observation of superconductivity for tungsten borides, WB and W_2B_4. Solid State Sci 14:1656–1659

[2] Cheng X-Y, Chen X-Q, Li D-Z, Li Y-Y (2014) Computational materials discovery: the case of the W–B system. Acta Crystallogr C70:85–103

[3] Cheng X, Zhang W, Chen X-Q, Niu H, Liu P, Du K, Liu G, Li D, Cheng H-M, Ye H, Li Y (2013) Interstitial-boron solution strengthened WB_{3+x}. Appl Phys Lett 103:171903

[4] Lech AT, Turner CL, Mohammadi R, Tolbert SH, Kaner RB (2015) Structure of superhard tungsten tetraboride: a missing link between MB2 and MB12 higher borides. Proc Natl Acad Sci USA 112:3223–3228

[5] Nagamatsu J, Nakagawa N, Muranaka T, Zenitani Y, Akimitsu J (2001) Superconductivity at 39 K in magnesium diboride. Nature 410:63–64

[6] Chung HY, Weinberger MB, Levine JB, Cumberland RW, Kavner A, Yang J-M, Tolbert SH, Kaner RB (2007) Synthesis of ultra-incompressible superhard rhenium diboride at ambient pressure. Science 316:436–439

[7] Turner CL, Taylor RE, Kaner RB (2015) ^{10}B and ^{11}B NMR study of elemental boron. J Phys Chem C 119:13807–13813

[8] Koumoulis D, Turner CL, Taylor RE, Kaner RB (2016) ^{11}B NMR spectral and nuclear spin–lattice relaxation analyses of ReB_2. J Phys Chem C 10:2901–2907

[9] Turner CL, Zujovic Z, Koumoulis D, Taylor RE, Kaner RB (2017) ^{11}B NMR study of WB_2. J Phys Chem C 121(2):1315–1320

[10] Burdett JK, Canadell E, Miller GJ (1986) Electronic structure of transition-metal borides with the AlB_2 structure. J Am Chem Soc 108:6561–6568

[11] Kopp JP, Barnes RG (1971) Nuclear magnetic resonance of ^{11}B and ^{27}Al in aluminum diboride. J Chem Phys 51:1840–1841

[12] Eastman M (1999) Examples of Hartmann–Hahn match conditions for CP/MAS between two half-integer quadrupolar nuclei. J Magn Reson 139:98–108

[13] Baek SH, Suh BJ, Pavarini E, Borsa F, Barnes RG, Bud'ko SL, Canfield PC (2002) NMR spectroscopy of the normal and superconducting states of MgB_2 and comparison to AlB_2. Phys Rev B 66:104510

[14] Papavassiliou G, Pissas M, Karayanni M, Fardis M, Koutandos S, Prassides K (2002) ^{11}B and ^{27}Al NMR spin–

lattice relaxation and Knight shift of $Mg_{1-x}Al_xB_2$: evidence for an anisotropic Fermi surface. Phys. Rev. B 66:140514(R)

[15] Pavarini E, Baek SH, Suh BJ, Borsa F, Bud'ko SL, Canfield PC (2003) NMR relaxation rates and Knight shifts in MgB_2 and AlB_2: theory versus experiments. Supercond Sci Technol 16:147–151

[16] Burkhardt U, Gurin V, Haarmann F, Borrmann H, Schnelle W, Yaresko A, Grin Y (2004) On the electronic and structural properties of aluminum diboride $Al_{0.9}B_2$. J Solid State Chem 117:389–394

[17] Choi YJ, Lu J, Sohn HY, Fang ZZ, Kim C, Bowman RC Jr, Hwang S-J (2011) Reaction mechanisms in the Li_3AlH_6/$LiBH_4$ and Al/$LiBH_4$ systems for reversible hydrogen storage. Part 2: solid-state NMR studies. J Phys Chem C 115:6048–6056

[18] Sevastyanova LG, Gulish OK, Stupnikov VA, Genchel VK, Kravchenko OV, Bulychev BM, Lunin RA, Tarasov VP (2012) Structure and properties of solid solutions in the Mg–Al–B system. Cent Eur J Phys 10:189–196

[19] Bielecki A, Burum DP (1995) Temperature dependence of ^{207}Pb MAS spectra of solid lead nitrate. An accurate, sensitive thermometer for variable-temperature MAS. J Magn Reson A 116:215–220

[20] Neue G, Dybowski C (1997) Determining temperature in a magic-angle spinning probe using the temperature dependence of the isotropic chemical shift of lead nitrate. Solid State NMR 7:333–336

[21] Beckmann PA, Dybowski C (2000) A thermometer for nonspinning solid-state NMR spectroscopy. J Magn Reson 146:379–380

[22] Jaeger C, Hemmann F (2014) EASY: a simple tool for simultaneously removing background, deadtime and acoustic ringing in quantitative NMR spectroscopy—part I: basic principle and applications. Solid State NMR 57–58:22–28

[23] Fenzke D, Freude D, Frohlich T, Haase J (1984) NMR intensity measurements of half-integer quadrupole nuclei. Chem Phys Lett 111:171–175

[24] Mann P, Klinowski J, Trokiner A, Zanni H, Papon P (1988) Selective and non-selective NMR excitation of quadrupolar nuclei in the solid state. Chem Phys Lett 151:143–160

[25] Ronemus AD, Vold RL, Vold RR (1986) Deuterium quadrupole echo NMR spectroscopy II. Artifact suppression. J Magn Reson 70:416–426

[26] Farrar TC, Becker ED (1971) Pulse and Fourier transform NMR: introduction to theory and methods. Academic Press, New York

[27] Yesinowski JP (2015) Finding the true spin–lattice relaxation time for half-integral nuclei with nonzero quadrupole couplings. J Magn Reson 252:135–144

[28] Harris RK, Becker ED, de Menezes SMC, Goodfellow R, Granger P (2001) NMR nomenclature, nuclear spin properties, and conventions for chemical shifts (IUPAC recommendations 2001). Pure Appl Chem 73:1795–1818

[29] Bishop M, Shahid N, Yang J, Barron AR (2004) Determination of the mode and efficacy of the cross-linking of guar by borate using MAS ^{11}B NMR of borate cross-linked guar in combination with solution ^{11}B NMR of model systems. Dalton Trans 17:2621–2624

[30] Bezhenar NP, Bozhko SA, Belyavina NN, Markiv VY, Shul'zhenko AA (2007) Кристаллическая структура диборида алюминия в композитах КНБ, полученных реакционным спеканием при высоких давлениях Dopov. Nats Akad Nauk Ukr 9:77–81

[31] Blaha P, Schwarz K, Madsen GK, Kvasnicka D, Luitz J (2001) WIEN2 k: an augmented plane wave + local orbitals program for calculating crystal properties. Tech Univ Wien, Austria. ISBN 3-9501031-1-2

[32] Perdew JP, Burke K, Ernzerhof M (1996) Generalized gradient approximation made simple. Phys Rev Lett 77:3865

[33] Tsiskarishvili GP, Lunström T, Tegenfelt J, Dolidze TV, Tsagareishvili GV (1991) Isotope effect in β-rhombohedral boron. In: AIP Conference Proceedings, pp 231–280

[34] Lee D, Bray PJ, Aselage TL (1999) The NQR and NMR studies of icosahedral borides. J Phys Condens Matter 11:4435–4450

[35] Sagalyn PL, Hofmann JA (1962) Nuclear magnetic resonance in metallic single crystals. Phys Rev 127:68–71

[36] Shyu W-M, Das TP, Gaspari GD (1966) Direct and core-polarization contributions to the Knight shift in metallic aluminum. Phys Rev 152:270–278

[37] Loa I, Kunc K, Syassen K, Bouvier P (2002) Crystal structure and lattice dynamics of AlB_2 under pressure and implications for MgB_2. Phys Rev B 66:134101

[38] Massiot D, Farnan I, Gautier N, Trumeau D, Trokiner A, Coutures JP (1995) ^{71}Ga and ^{69}Ga nuclear magnetic resonance study of β-Ga_2O_3: resolution of four- and six-fold coordinated Ga sites in static conditions. Solid State NMR 4:241–248

[39] Andrew ER, Tunstall DP (1961) Spin–lattice relaxation in imperfect cubic crystals and in non-cubic crystals. Proc Phys Soc 78:1–11

[40] Jung JK, Baek SH, Borsa F, Bud'ko SL, Lapertot G, Canfield PC (2001) ^{11}B NMR and relaxation in the MgB_2 superconductor. Phys Rev B 64:012514

[41] Lue CS, Tao YF, Su TH (2008) Comparative NMR investigation of the re-based borides. Phys Rev B 78:033107

[42] Ambrosini B (1999) An nmr study of anomalous rare-earth and actinide intermetalic compounds. Doctoral Dissertation

(Diss. ETH No. 13031), Swiss Federal Institute of Technology, Zurich

[43] Woesner DE, Timkin HKC (1990) The influence of MAS on spin–lattice relaxation curves and nuclear spin excitation of half-integer spin quadrupolar nuclei in solids. J Magn Res 90:411–419

[44] Yesinowski JP, Ladouceur HD, Purdy AP, Miller JB (2010) Electrical and ionic conductivity effects on magic-angle spinning nuclear magnetic resonance parameters of CuI. J Chem Phys 133:234509

[45] Spokas JJ, Slichter CP (1959) Nuclear relaxation in aluminum. Phys Rev 113:1462–1472

[46] Andrew ER, Hinshaw WS, Tiffen RS (1974) The anomalous ^{27}Al NMR second moment in metallic aluminum. J Phys F Metal Phys 4:L215–L218

[47] Wikner EG, Blumberg WE, Hahn EL (1960) nuclear quadrupole spin–lattice relaxation in alkali halides. Phys Rev 118:631–639

[48] Van Kranendonk J (1954) Theory of quadrupolar nuclear spin–lattice relaxation. Physica 20:781–800